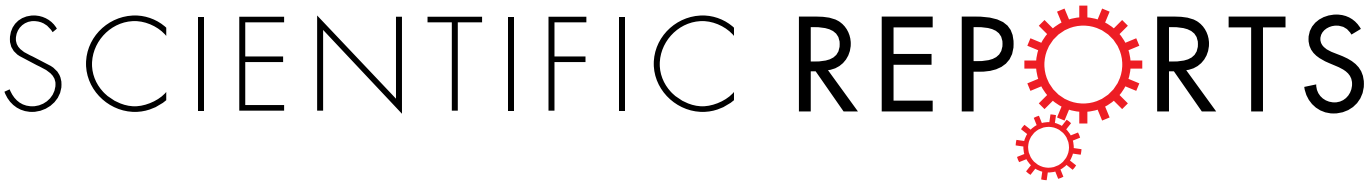

OPEN

Received: 11 August 2016
Accepted: 11 January 2017
Published: 13 February 2017

Superior adsorption and photoinduced carries transfer behaviors of dandelion-shaped Bi_2S_3@MoS_2: experiments and theory

Mengjiao Li, Junyong Wang, Peng Zhang, Qinglin Deng, Jinzhong Zhang, Kai Jiang, Zhigao Hu & Junhao Chu

The enhanced light-harvesting capacity and effective separation of photogenerated carriers in fantastic hierarchical heterostructures enjoy striking attention for potential applications in the field of solar cells and photocatalysis. A three-dimensional (3D) dandelion-shaped hierarchical Bi_2S_3 microsphere compactly decorated with wing-shaped few layered MoS_2 lamella (D-BM) was fabricated via a facile hydrothermal self-assembly process. Especially, polyethylene glycol (PEG) has been proven as the vital template to form D-BM microsphere. Importantly, the as-prepared D-BM microsphere presents pH-dependent superior adsorption behavior and remarkable visible light photocatalytic activity for degradation of organic dyestuffs (Rhodamine B/RhB and Methylene blue/MB), far exceeding those for the pure Bi_2S_3 and MoS_2. It is understandable that D-BM with high surface area possesses more active sites and promotes light utilization due to the unique porous structure with outspread wings. Besides, based on the experiments and theoretical calculations, the staggered type II band alignment of D-BM permits the charge injection from Bi_2S_3 to MoS_2, subsequently accelerates the separation and restrains the recombination of carriers, leading to excellent photocatalytic activity, as well as the photoconductance and photoresponse performance (with I_{light}/I_{dark} ratio 567).

The intense demand for photocatalysis applying to the pollutants degradation and the effective solar energy conversion keeps moving due to the worsening environment and energy crisis[1–9]. It is believed that the desired photocatalysis should have high light-harvesting capability and retardative recombination of photoexcited carriers[10–12]. A promising approach to enhance the photoactivity is to increase the light absorption range, the surface area and active site of the catalysts. Numerous studies have shed light on the importance of the semiconductor-based composites with certain modification in improving the performance, such as photovoltaic conversion, catalytic, and electrochemical properties[13–16]. Thus, studying the hierarchical semiconductor nanocomposite with controllable morphologies becomes the frontier strategy. Among these semiconductors, mater sulfides (ZnS, CdS) have been extensively surveyed for the generation of new optoelectronic performance with effective electron-hole separation and transport[5,14].

Typically, as a eco-friendly lamellar-structured semiconductor, Bi_2S_3, with a typical band gap (1.3–1.7 eV) for solar photovoltaic, has attracted lots of research interests[17–19]. In recent years, reported Bi_2S_3 nanocrystal with various morphologies have promising applications in solar cells, photodetectors, gas sensors, electrochemical hydrogen storage and X-ray computed tomography imaging due to the suitable band gap[20–23]. Besides, it also has been used as a stability sensitizer and photocatalyst derived from the broad absorption of visible light up to 800 nm[24,25]. However, the photocatalytic performance of Bi_2S_3 has been restricted because of the toilless recombination of photogenerated carriers and therewith the low quantum yield. Hence, as a feasible method so far to prolong the lifespan of electron-hole pairs, establishing composite structures with metal oxides, metal chalcogenides

Technical Center for Multifunctional Magneto-Optical Spectroscopy (ECNU), Shanghai Department of Electronic Engineering, East China Normal University, Shanghai 200241, China. Correspondence and requests for materials should be addressed to Z.H. (email: zghu@ee.ecnu.edu.cn)

or 2-dimensional (2D) hexagonal graphene, for instance Bi_2S_3/Bi_2WO_6, Bi_2S_3/TiO_2 and Bi_2S_3/Pd_4S, has been paid significant attention[12,26–29]. In particular, the 3-dimensional (3D) porous architecture with Bi_2S_3 skeleton, keeping superiority in large active contact area, is considered to have potential in synergistically enhancing the photocatalytic features.

The wide researches and successful applications of graphene recently have triggered great attention on 2D-layered materials. The 2D transition metal dichalcogenides (TMD) exhibit ultrathin physical characteristic, excellent optical, electronic, mechanical properties and potential applications in field-effect transitions (FET) and sensing devices[30–34]. As a representative 2D TMD, consisted of the weakly coupled S-Mo-S atoms sandwich layers, MoS_2 nanostructures have been synthesized with plentiful morphologies of nanosheet, nanoribbon and nanosphere[35–38]. Different from graphene, the controlled band gap (1.2–1.9 eV) and thermal stability, make MoS_2 be widely applied to biosensors, memory, capacitors, logic circuit devices, and lithium batteries[39–41]. Importantly, 2D-layered MoS_2 possesses a large surface area and massive active sites, which can provide sufficient contact and effective reactions[42]. Hence, forming hierarchical composites with MoS_2 has been proven to be promising and it also opens opportunities for optoelectronic applications. Zhou *et al.* have successfully fabricated MoS_2 nanosheet-coated TiO_2 nanobelt heterostructures, which showed a high photocatalytic hydrogen production and strong photocatalytic degradation of the dye molecules[31]. It is believed that the formation of this MoS_2-TiO_2 nanocomposite forcefully retard the photogenerated electron-hole recombination. Moreover, Chen *et al.* have put forward a bottom-up strategy of solvothermal method for 2D MoS_2 nanosheets composites, which exhibited preeminent properties in biomedicine and realized considerable applications in photothermal regression of tumor[43,44].

In this work, we propose a novel heterostructure of 3D-dandelion Bi_2S_3@MoS_2 microsphere using a facile hydrothermal method for the first time. Intriguingly, the layers of MoS_2 coating likes the wring of the dandelion. This unique architecture offered a high light utilization as a result of large surface area and massive active sites for reactions. Moreover, the formation of the staggered type II band alignment in D-BM made a prolonged lifespan of electron-hole pairs, based on calculated energy band positions and the corresponding electronic structures. Obviously, evaluated by the degradation of Rhodamine B (RhB) and Methylene blue (MB) under visible light, the as synthesized heterostructure exhibits more remarkable adsorption and visible light photocatalytic properties than the pristine Bi_2S_3 and MoS_2. Also, it presents improved photoresponse property with a high I_{light}/I_{dark} ratio of 567.

Results and Discussion

Phase structure and Raman studies. As shown in Fig. 1a, the phase information and purity of D-Bi_2S_3, MoS_2 nanoflowers and their composites were characterized by XRD analysis. Pattern I corresponded well to the lattice planes of orthorhombic Bi_2S_3 (JCPDS#65-2431 $a = 11.290$ Å, $b = 3.978$ Å, and $c = 11.150$ Å) without some impurity as Bi_2O_3. And pattern II can be indexed to the standard peaks of hexagonal MoS_2 (JCPDS#37-1492; $a = 3.16$ Å, $b = 3.16$ Å, and $c = 12.30$ Å). As for hierarchical D-BM structure (5 MBS, pattern III), the weak diffraction peak at $2\theta = 14.2°$, corresponding to the MoS_2 lattice plane of (002), can be inferred that the few-layered MoS_2 petals have been broken by D-Bi_2S_3. Raman spectroscopy was further utilized to identify the hybrid production. In Fig. 1b, two characteristic peaks of MoS_2 can be observed at 375 and 402 cm^{-1} from the local amplification, which correspond to the E_{2g} and A_{1g} vibration modes, respectively[41]. The vibrational modes of pure Bi_2S_3 microspheres are located at 107 cm^{-1} and 260 cm^{-1}, which can be assigned as the A_g and B_{1g} modes[21]. Obviously, all the characteristic Raman spectral signatures of Bi_2S_3 and MoS_2 both are presented in the result of their hybrids, demonstrating the successful incorporation of D-BM structures. Note that there is a blue shift of the B_{1g} mode compared to the pure Bi_2S_3. It probably suggests the surface strain is due to the novel coated MoS_2 on each Bi_2S_3 nanorod.

Morphology analysis. The morphology and micro-structure of all the samples have been investigated by SEM images. Figure 2a,b display the pure D-Bi_2S_3 microspheres in different magnifications. It can be seen that the Bi_2S_3 structures are distributed in the shape of irregular microspheres with the average diameter of 5 μm. Apparently (inset of Fig. 2b), these D-Bi_2S_3 micropheres were composed of a large number of acicular crystalline nanorods with uniform diameters of about 80 nm. Moreover, the broken D-Bi_2S_3 microsphere shown in Fig. 2c indicates that the acicular Bi_2S_3 nanorods radiate from the center and stack uniformly. It is extremely vital that the interstices between Bi_2S_3 nanorods can provide particular framework for the embedded of layered MoS_2 petals. As presented in Fig. 2d, the pure MoS_2 flowers reveal the diameter of 4 μm, with number of thinnish petals aggregated closely. The inset of Fig. 2d provides a chapped MoS_2 flowers, and it illustrates that these disordered petals grown from a common center to form the spherical structure. Figure 2e exhibits the morphology of the hydrothermal synthesized D-BM (5 MBS) hetero-microspheres. Detailedly, some other SEM information on Bi_2S_3, MoS_2, and hybrids are shown in Figs S1 and S2 (ESI). Generally, the whole D-Bi_2S_3 microspheres are uniformly covered with 2D MoS_2 nanosheets. A high magnification top view SEM image shown in the inset of Fig. 2e, the composites present apparent differences from the pristine D-Bi_2S_3 or MoS_2. Iconically, almost each Bi_2S_3 nanorod are compactly decorated with a pair of expanding wings of MoS_2 nanosheets, thus forming the MoS_2 coated Bi_2S_3 heterostructure. In the inset of Fig. 2f, a section of the broken composites elucidates that MoS_2 nanosheets have grown along the Bi_2S_3 nanorods and deeply rooted in the center of Bi_2S_3 spheres, which expects that this unique hierarchical architecture can provide more effective activity sites and enhance the photoelectric properties.

In addition, a sequence of TEM and HRTEM images of D-BM nanocomposite have been employed to reveal more specific structural information. In Fig. 3a, homogeneous MoS_2 sheets are detected at the edge of each Bi_2S_3 nanorod from the low magnification TEM survey. Not only Fig. 3b,c clarify the intimate interfacial contact between MoS_2 sheets and elongated Bi_2S_3 rods, but also they indicate that the MoS_2 sheets are ultrathin compared with the pure MoS_2 flowers. In the HRTEM image (Fig. 3e), the lattice fringes of $d = 3.54$ Å and $d = 3.74$ Å,

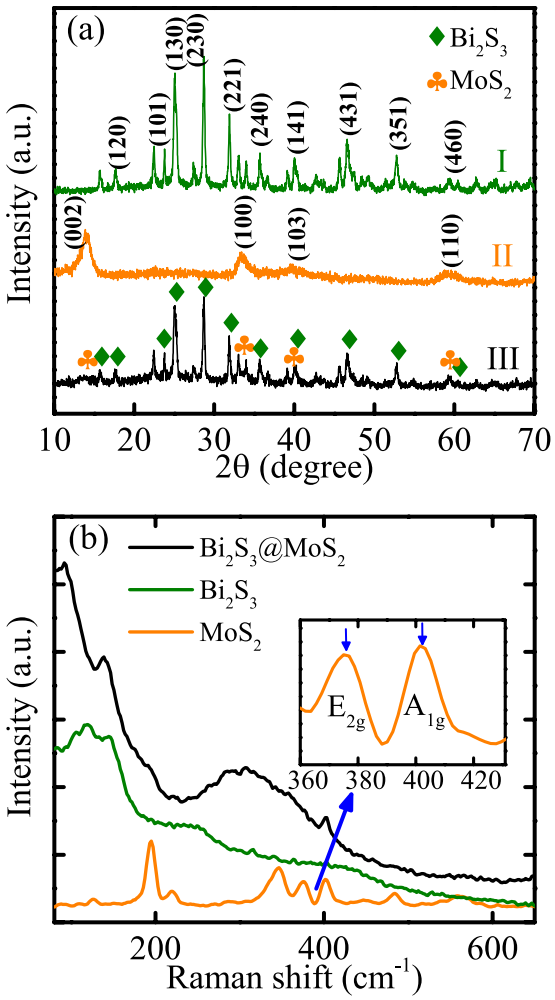

Figure 1. (**a**) XRD patterns and (**b**) Raman spectra of pristine of Bi_2S_3, MoS_2, and the D-BM composites. The inset shows both E_{2g} and A_{1g} Raman modes of MoS_2.

corresponding to the (130) and (101) planes of Bi_2S_3, respectively[28]. The coated MoS_2 exhibits the lattice spacing of 6.19 Å, which matches well with the (002) planes of hexagonal MoS_2[31]. Furthermore, the related cleaved crystal structure in theoretical section indicates the distance between adjacent Bi atoms on the (130) crystal surface of Bi_2S_3 (3.4148 nm), which is eleven intervals of the adjacent S atoms on the (001) crystal surface of MoS_2 (0.3169 nm × 11)[45]. It is believed that Bi_2S_3 nanorods might be available for the growth of the MoS_2 nanosheets to form the heterostructure between the mutual effect of S and Bi atoms. Thus, it can be inferred that the MoS_2 sheets, with about 5–8 layers, embellished at the surface of the Bi_2S_3 rods. Moreover, the selected area electron diffraction (SAED) pattern (inset of Fig. 3b) further proves the mixed-phase nature of single crystal Bi_2S_3 (bright diffraction spots) and layered superimposed MoS_2 sheets (diffraction rings). In order to accurately confirm the elemental composition and spatial distribution, energy dispersive X-ray spectrometry (EDS) analysis in Fig. 3e have been performed. The well-proportioned distributions of S, Bi, and Mo can be obtained from the mapping results. Besides, the EDS line scan (Fig. 3f) of the marked region sheds light on the unique hierarchical heterostructure, as well as in agreement with SEM and TEM observation.

XPS analysis. We also performed XPS analysis to elucidate the surface chemical composition and valence states of the pristine Bi_2S_3, MoS_2, and D-BM (5 MBS) heterostructures. The Fig. 4a shows the survey XPS spectra of Bi_2S_3 and MoS_2 (Note that C element acts as reference and O element comes from the absorbed oxygen). After the second hydrothermal reaction, the overall XPS spectra in Fig. 4b indicates the main constituent of Bi, S, and Mo elements. Figure 4c,d display the spin-orbit components of Bi 4*f* (158.46/163.76 eV) and Mo 3*d* (228.84/231.99 eV) for pure Bi_2S_3 and MoS_2, respectively. In addition, the XPS spectrum of the hybrids in Fig. 4e can be well fitted into several dominate peaks with binding energies of 158.75 eV, 162.05 eV, 163.30 eV, and 164.05 eV, which are assigned to Bi $4f_{7/2}$, S $2p_{3/2}$, S $2p_{1/2}$, and Bi $4f_{5/2}$, respectively. The high resolution Mo 3*d* (Fig. 4f) binding energies of the hybrids are located at around 229.23 eV and 232.38 eV, corresponding to Mo $3d_{5/2}$ and Mo $3d_{3/2}$, respectively. Notablely, the Bi 4*f* and Mo 3*d* peaks shift toward the high banding energy, with dotted lines mark. Hence, it could be deduced that chemical bonds of Bi-S-Mo formed probably, related to the electronic shielding effect[46]. A weak peak at 226.31 eV has also be found (Fig. 4f), which is attributed to the S 2*s*[47].

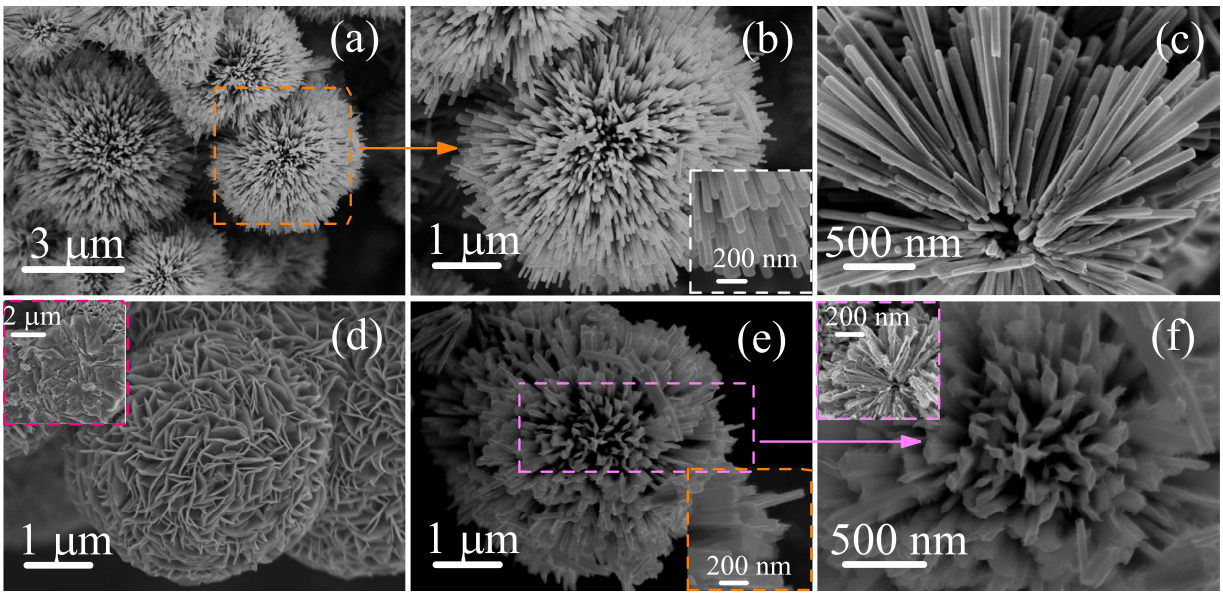

Figure 2. (**a**,**b**) SEM images of the dandelion-shaped Bi_2S_3 microspheres under different magnifications. The inset shows the high magnification SEM image of vimineous Bi_2S_3 nanorods. (**c**) The broken Bi_2S_3 microspheres. (**d**) SEM image of MoS_2 nanoflower and the inset is the several chapped MoS_2 nanoflowers. (**e**,**f**) SEM image with different magnifications of the synthesized D-BM heterostructures. The insets are a local amplification from the side views and a broken section.

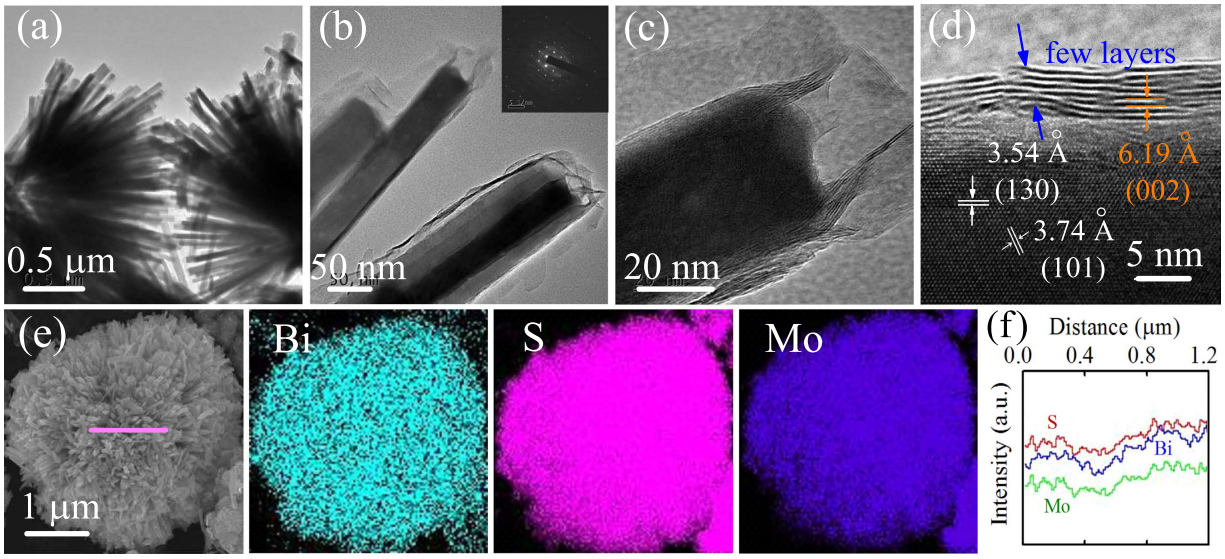

Figure 3. (**a**) TEM image of D-BM microstructures. (**b**) The surface of D-BM and the inset is the SAED pattern. (**c**,**d**) HRTEM images of D-BM. (**e**) SEM image of D-BM and the corresponding EDS mapping images of Bi, S, and Mo elements. (**f**) The corresponding EDS line scan along the pink line in (**e**).

Take the spin orbit separation into consideration, the phenomenon among Bi 4*f* (5.30 eV), S 2*p* (1.25 eV), and Mo 3*d* (3.15 eV) peaks disclose the existence of Bi^{3+}, S^{2-}, and Mo^{4+}, based on the reported results.

Growth mechanism investigation. The growth mechanism of the D-BM nanomaterials has been studied for potential applications and controllable synthesis of other novel structures. For D-Bi_2S_3, the formation process has been investigated by SEM at different reaction times, as shown in Fig. 5a–f. At the early reaction stage (1 h), the half-baked microspheres (diameter of 2 μm) have been formed and proven to be orthorhombic Bi_2S_3 by XRD analysis (Fig. S3), which indicate the fast nucleation of Bi_2S_3. As the reaction proceeded (3 h), some actinomorphic-shaped Bi_2S_3 (diameter of 5 μm) can be captured in Fig. 5b. From the close inspection (Fig. S4), however, the surface of the radial Bi_2S_3 nanorods are rough and inhomogenous, indicating a rapid growth of Bi_2S_3 microspheres. By prolonging the reaction time to 8 h, massive intact D-Bi_2S_3 microspheres have been successfully

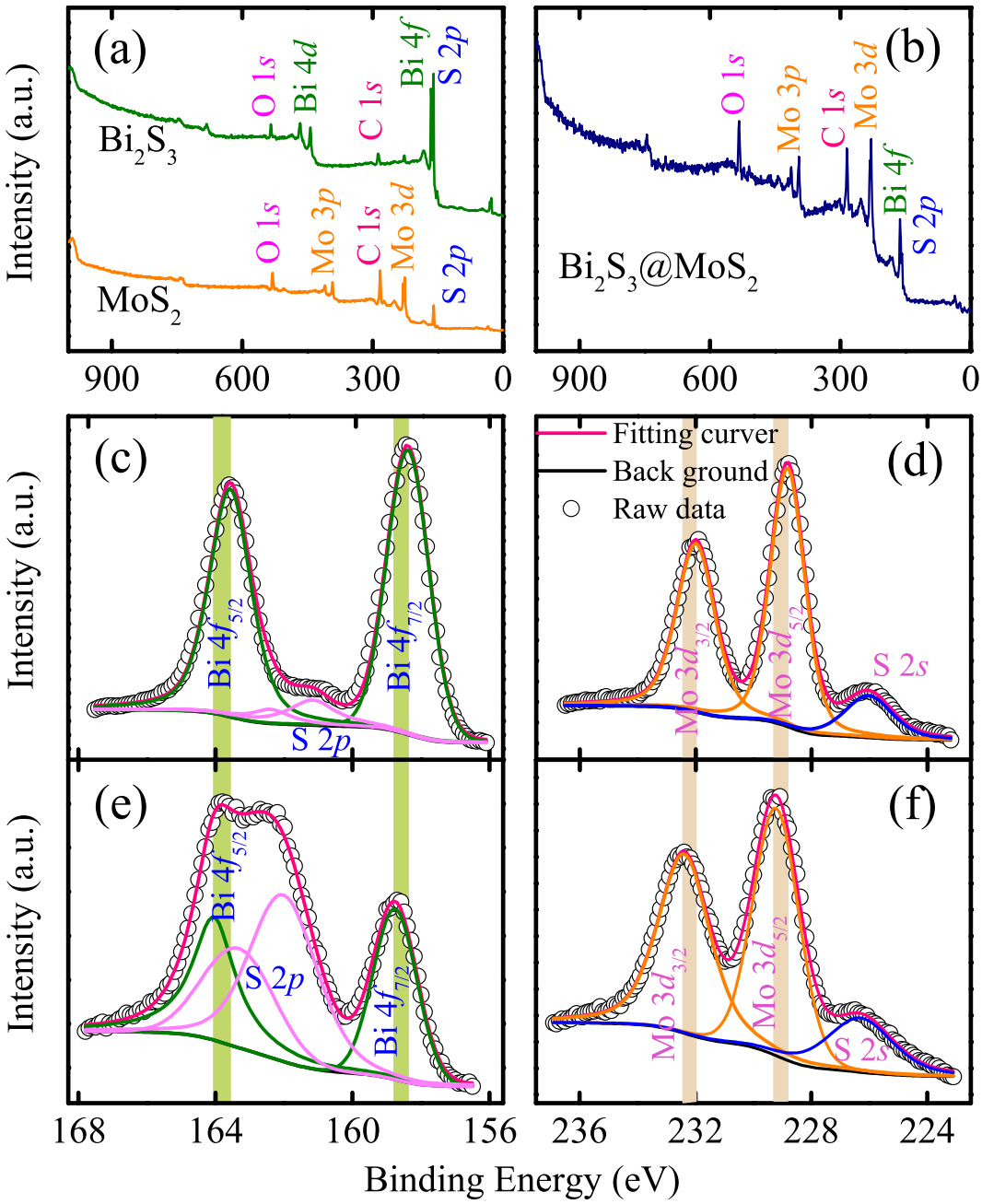

Figure 4. XPS spectra of as-synthesized products. (**a**,**b**) The overall spectra of Bi_2S_3, MoS_2, and 5 MBS, respectively. The Bi 4*f* and Mo 3*d* spectra for Bi_2S_3 (**c**), MoS_2 (**d**), and D-BM (**e**,**f**), respectively. Note that the scatter and solid lines indicate the experimental data and fitting results, respectively. The dotted lines mark the peak shifts of Bi 4*f* and Mo 3*d*.

synthesized. Then the products under hydrothermal condition have been collected at 5 h, 8 h, and 12 h. The SEM images in Fig. 5d–f manifest that the coated MoS_2 nanosheets become increasing and orderly along with the prolonged reaction process. It can also be verified through the related XRD survey (Fig. S4). At the beginning, the characteristic peak of MoS_2 at $2\theta = 14.2°$ is indeed indetectable. With prolonging the reaction time, the emergence of MoS_2 (002) plane provides the convincible proof for the formation of the MoS_2 coated Bi_2S_3 nanocomposites.

Based on the results of the time-dependent experiments and analysis, the probable morphology evolution process of the hetero-Bi_2S_3@MoS_2 structure is illustrated in Fig. 5g. In our experiments, thiourea was chosen to act as the sulfide source, for constituting the Bi^{3+}-thiourea complexes, initially. Under elevated temperature, these complexes decomposed, accompanied by shaping into needle-like nanospheres with nucleated Bi_2S_3[48,49]. As time went on, Bi_2S_3 grew gradually to improve the rough surface, at the expense of Bi_2S_3 particles or rods. It can be attributed to the typical Ostwald ripening process, which could significantly reduce the total surface free energy[50]. Besides, the solution of PEG is necessary to build a suitable viscous surroundings, which promotes the unique geometrical patterns. For comparison, the morphology and crystallinity of the product obtained without PEG

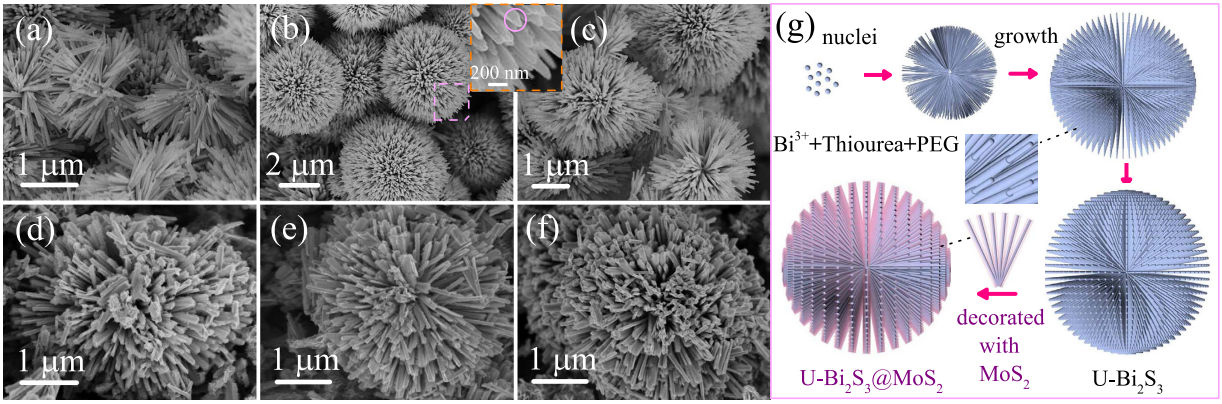

Figure 5. (**a**–**c**) SEM images of the Bi_2S_3 products fabricated at 1 h, 3 h, and 8 h, respectively. (**d**–**f**) SEM images of the D-BM products obtained at 5 h, 8 h, and 12 h, respectively. (**g**) Schematic illustration of the morphological evolution process of D-BM hybrids.

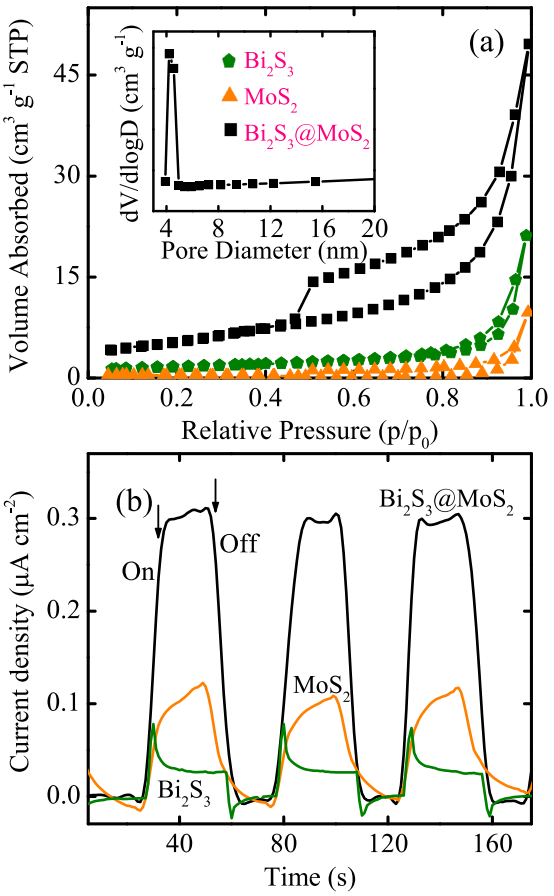

Figure 6. (**a**) Nitrogen adsorption-desorption isotherms and the pore-size distribution (inset) of the as-synthesized samples. (**b**) Comparison of transient photocurrent responses of the as-prepared products illuminated by simulated sunlight.

also have been surveyed. As a result (Fig. S5), the regular Bi_2S_3 microspheres with short tomentum ascertain the role of PEG as the important template. Finally, the 3D D-Bi_2S_3 microspheres could provide available high active sites for the growth and insertion of MoS_2 nuclei, leading to the hierarchical and porous framework.

BET surface areas and photocurrent response. As shown in Fig. 6a, the nitrogen adsorption-desorption measurements have been performed to ascertain the surface area and the porous structure of the as-synthesized samples. According to the Brunaner-Deming-Deming-Teller (BDDT) classification, the isotherms of D-BM displays a typical hysteresis loops as type IV. The specific Brunauer-Emmett-Teller (BET) surface area have been

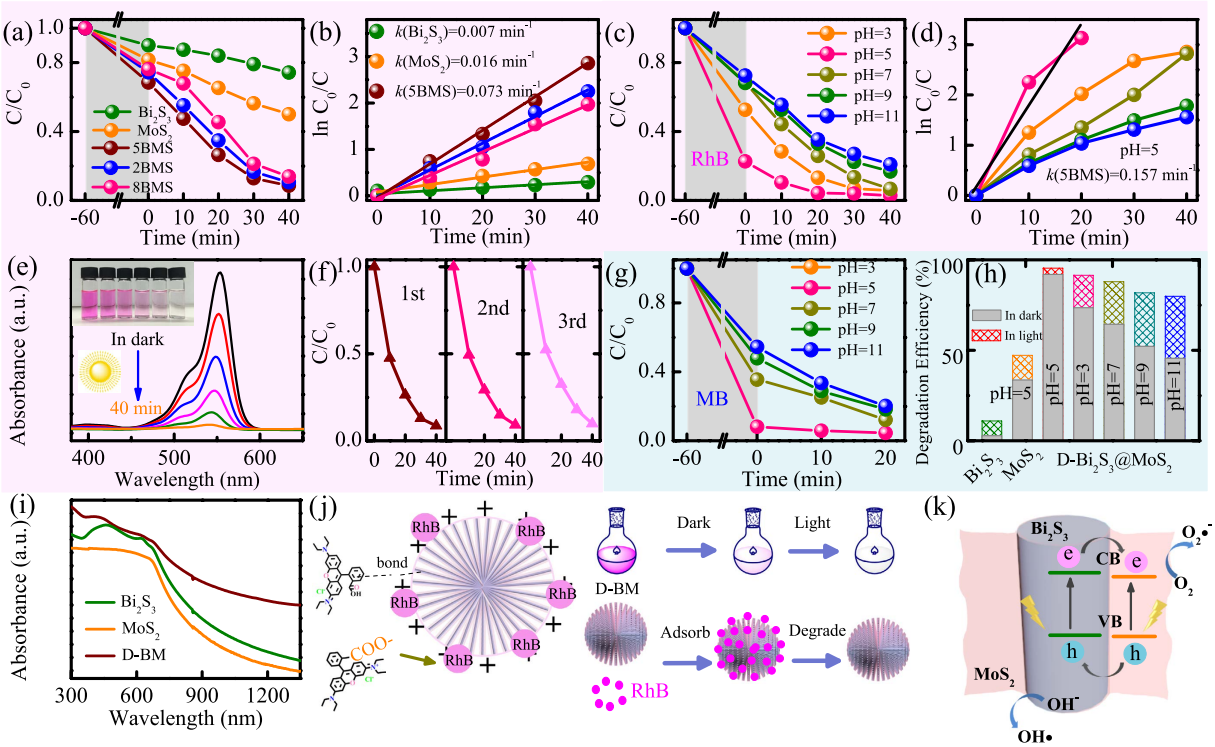

Figure 7. The adsorption (in dark) and photodegradation (visible light irradiation) effects (C/C_0) of RhB aqueous solution (10 mg/L) at (**a**) pH = 7 by different catalysts and (**c**) pH = 3–11 by D-BM. The plots of $ln(C_0/C)$ *versus* irradiation time of RhB aqueous solution at (**b**) pH = 7 by different catalysts and (**d**) pH = 3–11 by D-BM. The corresponding adsorption spectra (**e**) and photodegradation ((**f**), cycled catalyst) of RhB solution after 60 min in dark and 40 min irradiation with D-BM at pH = 7. The adsorption (in dark) and photodegradation (visible light irradiation) effects (C/C_0) of MB aqueous solution (10 mg/L) at (**g**) pH = 3–11 by D-BM and (**h**) the corresponding decomposition rate by different catalysts. (**i**) The absorption spectra of the catalysts. (**j**) Relevant kinetics mechanism of adsorption and photocatalysis for D-BM in RhB solution. (**k**) Schematic diagram of the charge transfer and separation mechanism for the D-BM heterostructure.

estimated to be about 19.48 m^2/g for the hybrid. Obviously, the characteristics with enlarged surface area and porosity of the composite recognized the embedded structure of MoS_2 nanosheets into Bi_2S_3 microspheres. By the Barrett-Joyner-Halenda analysis, the pore-size distribution of Bi_2S_3@MoS_2 (inset of Fig. 6a) indicates the main mesopores with about 4.5 nm.

Before moving toward the photocatalytic study of the as-synthesized products, the separation of charge carriers, as a crucial factor, needs to be investigated indispensably. Hence, the photocurrent transient response measurements of pure Bi_2S_3, MoS_2, and their mesoporous composites have been carried out to verify the extended lifespan of the photogenerated charges. Under visible-light irradiation, Fig. 6b records the fast and consistent photocurrent responses over several on-off cycles, illustrating that all three samples are reproducible and stable. Apparently, pure Bi_2S_3 and MoS_2 both present low photocurrent densities, consisted with the low quantum efficiency. However, the photocurrent density of the D-BM electrode is enlarged about one order of magnitude higher than the pure Bi_2S_3 electrode. It can be interpreted that this novel heterostructure possess particular tunnel for transformation of photogenerated carries, subsequently retards the recombination and extends the lifetime of carries.

Adsorption and photocatalytic properties. To demonstrate the photocatalytic ability of the D-BM heterostructures, photodegradation of RhB in aqueous solution has been investigated under visible-light irradiation. In Fig. 7a, at pH = 7, the corresponding decomposition rate of bare Bi_2S_3 (26%) and MoS_2 (50%) are indistinctive after 40 min. Whereas, when the MoS_2 was introduced to Bi_2S_3, the decomposition rate significantly increases to near 92%. The time-dependent absorption spectra of RhB solutions by D-BM and others were shown in Fig. 7e and Fig. S6. It could conclude that the hierarchical D-BM structure owns outstanding photocatalytic performance than two others. As it has been proposed by Daage, the "rim-edge" mode of MoS_2 have massive dege active sites, where strong interaction occurs with dye molecules[51–53]. Also, these ultrathin and wrinkled surfaces of MoS_2 may lead to several internal intersections, which make it possible to bring much more effective area for absorption. Likewise, it is favoring to transfer excited carries between MoS_2 and Bi_2S_3 heterostructure, leading to reduce the recombination efficiency and prolong the lifetime of carries. In addition, the photocatalytic activity can also be related to the amount of the coated MoS_2 nanosheets, which highlights the optimization of 5 MBS. As for 2 MBS samples, fewer MoS_2 nanosheets cannot provide enough multiplex refraction for the incident path, as well as

the more active site for the adsorption of reactant molecules. On the other hand, 8 MBS samples with superabundant MoS_2 nanosheets impeded the transformation of photogenerated carries in reverse, thus facilitating their recombination. To make a more specific comparison, the reaction kinetics of all catalysts have been linear fitted as $\ln(C_0/C) = kt$ according to Landmuir-Hinshelwood mechanism shown in Fig. 7b [54–56]. Note that C and C_0 are the real-time concentrations and initial concentration of RhB, t and k denote the irradiation time and the overall photodegradation rate constant, respectively. The rate constant of pristine Bi_2S_3 and MoS_2 are 0.007 and 0.016 min^{-1}. Nevertheless, a dramatic improvement (0.073 min^{-1}) of 5 MBS can be achieved. Specifically, the increased reaction rates were attributed to the unique porous structure, with faster mass transport and more accessible active sites, resulting in an increased reaction rate. The stability and reusability of the composites (sample 5 MBS at pH = 7) also have been evaluated under irradiation by collecting and reusing them over 3 cycles. As shown in Fig. 7f, the insignificant decline in photocatalytic activity after three runs (90%) confirms the stability of the catalysts, excepting the incomplete collection. The constancy can be recognized through the XRD result after photocatalytic tests (Fig. S7).

It is believed that the effective photocatalysis need handle both the mass transfer and the light transfer issues. The adsorption capacity of catalyst surface for dyes during illumination is a defining factor in photodegradation. In addition, the initial pH plays a dominant role to the adsorption process. Therefore, based on the above adsorption behavior of the D-BM product in dark and neutral surroundings, the pH-dependent adsorption (3.0–11.0) and photocatalysis survey have been conducted. Note that the initial pH of the RhB solution was adjusted by HCl and NaOH solution (1 M). The Fig. 7c reveals that the adsorption capacity of D-BM hybrids has been promoted under acidic conditions and pH = 5 appears to the most beneficial. The adsorption efficiency reaches approximately 76% (Fig. S8) and photodegradation rate $k = 0.157\ min^{-1}$ (Fig. 7d) at pH = 5. For verifying the adsorption behavior and photocatalytic activity of D-BM hybrid, the colors of the degraded MB solutions (Fig. S8) and photodegradation of MB solution under pH of 3, 5, 7, 9, and 11 have been obtained in Fig. 7g,h. Obviously, D-BM shows a superior adsorption and photodegradation properties compared with pure Bi_2S_3 and MoS_2, especially when pH < 7. Accordingly, although the initial pH affects the adsorption process of dyes onto the catalyst, the photodegradation process of D-BM remains resultful at a large range of pH values. It indicates that D-BM hybrid can serve as a high efficiency catalyst for wastewater treatment, which contained a mild acid commonly.

In order to further investigate the stability of the catalyst, the XRD and EDS mapping results after adsorption and photodegradation tests have been shown in Fig. 8a,b. Compared with the XRD results (Fig. 1a) and EDS mapping (Fig. 3e) before photocatalysis, there exist minor change among the elemental composition, spatial distribution, and the phase characterization results. Therefore, the composite has presented relative stability in view of its unique heterostructure and synergistic effect attributed to the intense interaction between Bi_2S_3 and MoS_2, which favors the separation of the photoinduced carriers. However, a small percentage of the samples might had undergone hydrolysis which was unavoidable, taking the slight decrease through cycling experiments and photocorrosion into consideration.

Relevant kinetics mechanism. In Fig. 7j,k, the related adsorption and photocatalysis kinetic mechanism of the D-BM heterostructure under visible light irradiation has been put forward. In mild acidic environment (pH < 7), the surfaces of the catalyst is exposed to acidic (positive) conditions and positively charged, as shown in Fig. 7j. In addition, both the π-bond of RhB and MB can beneficially excite electrons with irradiation, as well as the existence of the functional groups ($-COO^-$) as the shown molecular structure of RhB in Fig. 7j. Thus, we can conclude that the dyes might be adsorbed by D-BM hybrid through complex relationship involving electrostatic attraction or hydrogen bonds. Subsequently, these adsorbed dyes on the surface of D-BM could be *in situ* degraded promptly (Fig. 7j). The mass transfer and the chemical reaction process can be guaranteed by the opposite concentration difference and the visible light irradiation, which help to accomplish the degradation synergistically. In order to make it clear, the right part of the Fig. 7j illustrates the complete process simply, which contains both the adsorption and the photocatalysis behaviors of the D-BM hybrid.

On the other hand, since the band-edge potential levels play a crucial role in determining the migration directions of the photoexcited carriers in a heterojunction, the relative band positions of the two semiconductors have been investigated to approach the mechanism of the enhanced photocatalytic activity of their composites. Significantly, a staggered type-II configuration formed at the interface of D-BM structures by the calculated band edge positions, according to the empirical formula: $E_{VB} = X - E_e + 0.5E_g$ [12]. Note that E_{VB} is the valence band (VB) edge potential and E_e refers to the free electrons energy based on the hydrogen scale (4.5 eV). Based on previous studies, X is the electronegativity of the corresponding semiconductor (5.28 eV for Bi_2S_3 and 5.32 eV for MoS_2), expressed as the geometric mean of the electronegativity for the component atoms, and the band gap energy E_g of Bi_2S_3 and MoS_2 are 1.33 eV and 1.3 eV, respectively [12,19]. Correspondingly, the E_{VB} and E_{CB} (CB, the conduct band) of Bi_2S_3 are estimated to be 0.12 eV and 1.45 eV, both higher than those of MoS_2, with $\Delta E_{VB} = 0.02$ eV and $\Delta E_{CB} = 0.05$ eV, respectively. Compared with the pure samples, the heterostructure of D-BM presents an obvious enhanced absorption (Fig. 7i), both in range and intensity. As illustrated in Fig. 7k, under visible-light irradiation, excited electrons-holes are generated facilely in both Bi_2S_3 and MoS_2. With the suitable type II band alignment, the transfer of carries are also performed from the CB of Bi_2S_3 to MoS_2, as well as the reflux of holes mainly from the VB of MoS_2 to Bi_2S_3. Therefore, more vacancies have been left at the bottom of CB and top of VB for Bi_2S_3/MoS_2, resulting in pronging the lifetime of carries and boosting more available separation. After the photoexcited carries fleetly flow to the CB of MoS_2, the reaction of $O_2 \rightarrow O_2\bullet^-$ has been further promoted through one-electron reducing. Then hydroxyl radicals OH•, the dominating active species of RhB photodegradation, can be generated by the reaction between water and the unstable superoxide radical anion $O_2\bullet^-$ [57]. Meanwhile, the remaining holes in the valence band of Bi_2S_3 also participate in the degradation of RhB as the trapped active species.

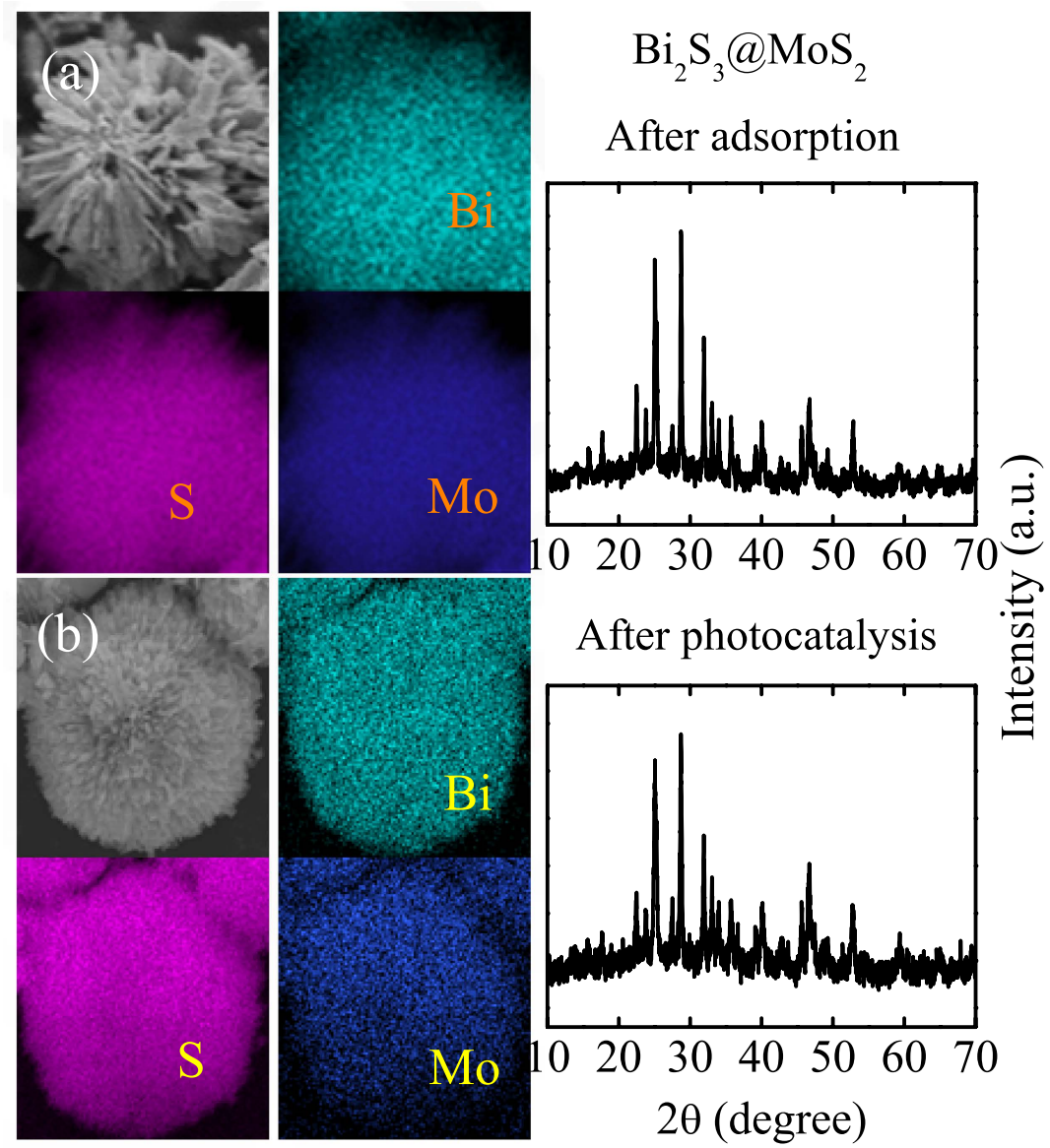

Figure 8. The EDS mapping and the corresponding XRD results after (**a**) adsorption and (**b**) photodegradation tests.

Photoconductance and photoresponse performances. Besides photocatalysis, the as-synthesized D-BM hybrid is expected to have improved photoconductance and photoresponse properties compared with the pure Bi_2S_3 structure. In order to spin coating, the photodetector devices (Fig. 9a) were fabricated by these disrupt NR-BM and Bi_2S_3 nanorods (NR-Bi_2S_3). Figure 9b plots the typical current-voltage (I–V) curves of NR-BM based nano-photodetector exposed to 650 nm illumination (1.0 mW cm^{-1}) and in dark, respectively. It is obvious that the quasilinearity of the I–V curves indicates the formation of an good Ohmic contact between Au electrode and NR-BM interface. With illumination, the NR-BM shows a remarkable photocurrent reaches about 0.703 μA under −1.5 V bias voltage, resulting a higher I_{light}/I_{dark} ratio to about 567, which compared to the NR-Bi_2S_3 of 126 with the shortened lifetime of the electron-hole pairs (Inset of Fig. 9b). The electrical characteristics of the NR-BM based device have been investigated in dark and at increasing illumination intensities from 0.25 mW cm^{-1} to 5 mW cm^{-1} (Fig. 9c). Clearly, the photocurrent increases with the enlarged light intensity and exhibits a high dependence on it, and their relationship can be described by a simple power law as $I = AP^{\theta}$[58,59]. Where A and θ represent a constant for a certain wavelength and the response of photocurrent to light intensity, respectively. The fitting curve leads to θ = 0.89, which suggests that there exists little trap states (Inset of Fig. 9c) in the NR-BM photodetector. In addition, Fig. 9d provides the time dependent photoresponse of the D-BM device at a bias voltage of 1 V, which sheds light on a readily switch between high- and low-conduction states by illumination on/off. It is known that the responsivity (R) serves as a critical metric to the photodetector sensitivity, which is defined as $R(AW^{-1}) = I_p/P_{opt}$[60]. Where I_p and P_{opt} are the photocurrent and incident light power, respectively. Based on the results, the R of the D-BM device is estimated to be 13.3 AW^{-1}. Consequently, the improvement of

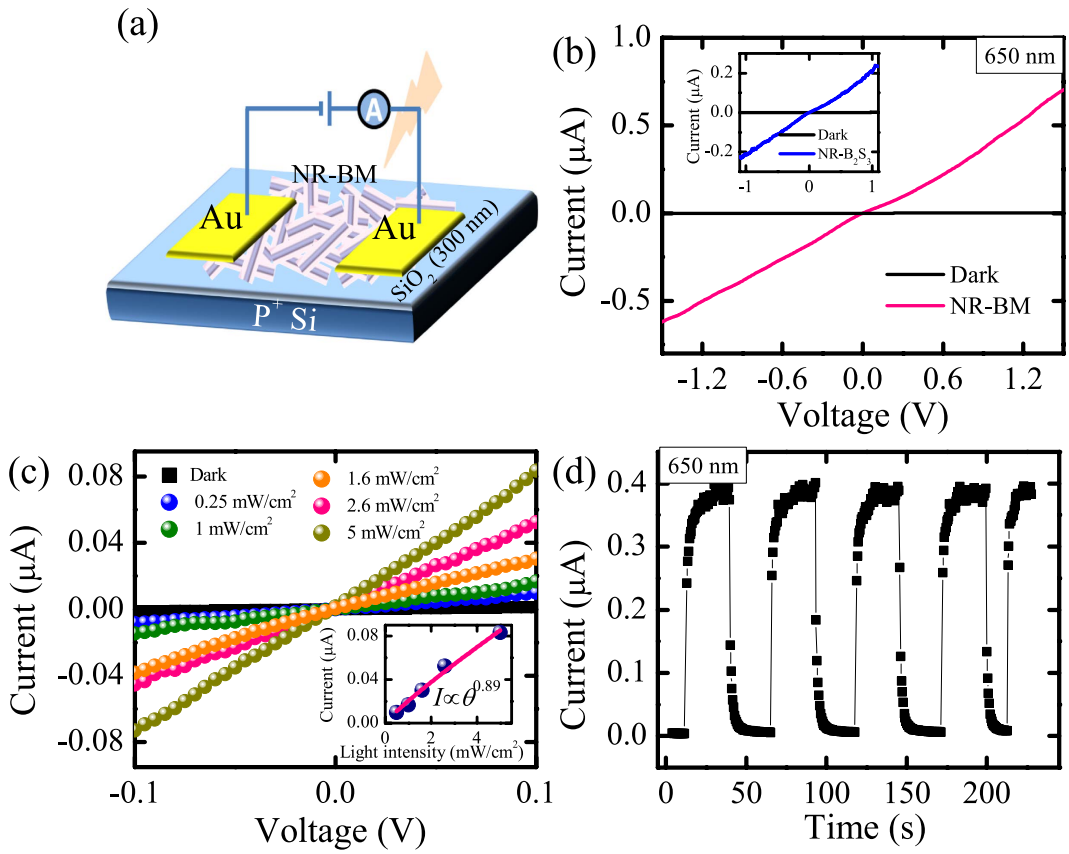

Figure 9. (**a**) Schematic illustration of the fabricated photodetector. The I-V curves of the NR-BM (Inset of Fig. 8b for NR-Bi_2S_3) photodetectors illuminated by 650 nm with (**b**) 1.0 mW/cm^2 and (**c**) different incident light intensity. Inset of Fig. 8c is the photocurrent measured *versus* light density at a bias voltage of 0.1 V. (**d**) The time dependent of the on-off photocurrent response of the device at a bias of 1 V by 650 nm illumination.

photoconductivity and photoresponse performance supports the efficient carries separation resulting from the heterostructures of dandelion-shaped Bi_2S_3@MoS_2.

Theoretical investigation. The obtained band structures and the density of states (DOS) of Bi_2S_3 and MoS_2 have been shown in Fig. 10a–f, respectively. As we can see, the top of VB contains S 3*p* and few contributions of Bi 6*s*, while the bottom of CB are mostly Bi 6*p* and S 3*p* for Bi_2S_3, with calculated $E_g = 1.44$ eV. As for MoS_2 (with calculated $E_g = 1.29$ eV), the top of VB originates from Mo 4*d*, and the bottom of CB are Mo 4*d* and some hybridization with S 3*p*. Note that Fig. 10f shows the crystal surface matching of MoS_2 (top) and Bi_2S_3 (down). By aligning the Fermi level relative to the vacuum energy level, the obtained work functions for Bi_2S_3 and MoS_2 are 4.88 and 5.00 eV, respectively. Due to the differential work functions, a built-in electric field from Bi_2S_3 to MoS_2 can be established near the interface. Thus the built-in electric field of the composites is expected to facilitate the separation of photo-generated carriers. It can be concluded that the theoretical calculations of the band energy positions (Fig. 10e) keep highly unanimous with the experimental results. In consequence, the MoS_2 nanosheets uniformly layered-coated the Bi_2S_3 microspheres sufficiently absorb visible-light and retard the electron-hole recombination, eventually leading to improvement of the photocatalytic and optoelectronic properties. Moreover, the unique novel architecture can provide valuable references to take advantage of solar energy in the future.

Conclusion

In summary, a green strategy based on the hydrothermal method has been developed for the fabrication of hierarchical 3D dandelion-shaped Bi_2S_3 microspheres coated with layered MoS_2 nanosheets. The novel heterostructure with unique porosity and intimate interfacial contact can provided efficient visible-light utilization and penetrable paths for reactant molecules to reach the inner structure. Compared with the pristine Bi_2S_3 or MoS_2, the as-synthesized D-Bi_2S_3@MoS_2 composite has exhibited much higher adsorption behavior and photocatalytic activity under visible-light irradiation. The formed staggered type II band alignment of Bi_2S_3@MoS_2 has expected to promote the separation of carries, accelerate the transportation and prolong lifespan of electron-hole pairs, which can be verified by the excellent photoconductance and photoresponse properties. Correspondingly, the Bi_2S_3@MoS_2-0.5 mol (5 MBS) has been proven to achieve an optimal photocatalysis performance, highlighting the importance of novel core/shell heterostructures for environmental remediation and solar energy harvesting applications in the future.

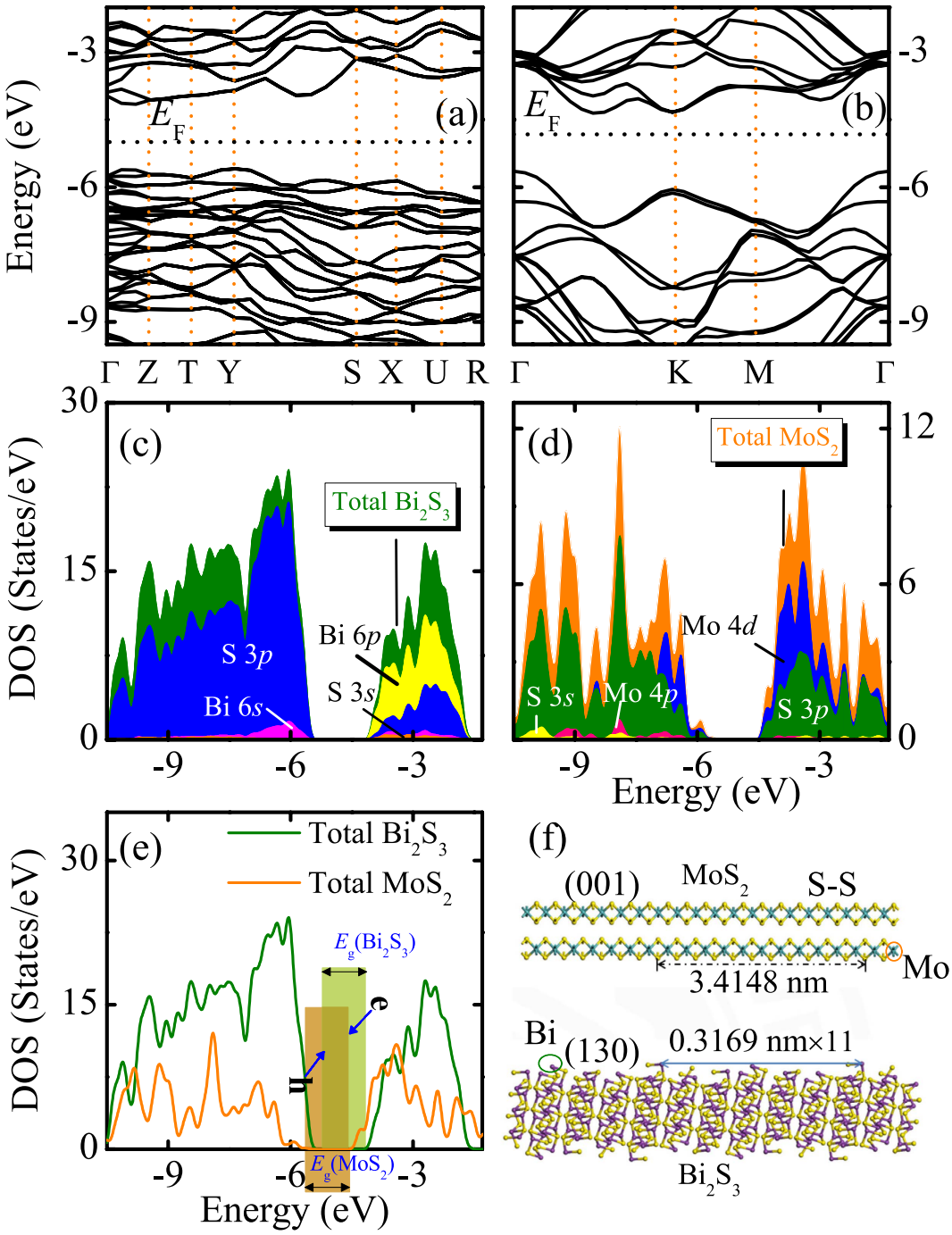

Figure 10. Calculated band structures (**a**,**b**), the density of states (**c**–**e**), and the crystal surface matching between the (130) and (001) crystal surfaces (**f**) of Bi_2S_3 and MoS_2, respectively.

Methods

Synthesis. Generally, the D-BM heterostructure were synthesized by a two-step hydrothermal method. Firstly, the dandelion-shaped Bi_2S_3 microspheres were prepared at 180 °C[19]. Then, for forming the hybrids, another hydrothermal process was employed to embed MoS_2 nanosheets onto Bi_2S_3 microspheres (molar ratios of Mo^{4+} to Bi^{3+} were 20%, 50%, and 80%, with the labels of 2 MBS, 5 MBS, and 8 MBS, respectively). Further information about the experimental details are available in the ESI.

Characterization. The crystallinity and purity of the resulting products were assessed by X-ray diffraction (XRD, Bruker D8 Advance diffractometer) equipped with Cu Kα radiation ($\lambda = 1.5418$ Å). Field emission scanning electron microscopy (FESEM, JEOL-JSM-6700F) was employed to investigate the morphologies of the synthesized samples, equipped with an energy dispersive X-ray spectroscopy (EDS). For detailed insight into the 2D-layered MoS_2 coated Bi_2S_3, Transmission Electron Microscope (TEM) and high resolution transmission

electron microscopy (HRTEM) studies were analyzed at the accelerating voltage of 200 kV. X-ray photoelectron spectroscopy (XPS, RBD upgraded PHI-5000C ESCA system, Perkin-Elmer) measurements were carried out with Mg-Kα radiation ($h\nu = 1253.6$ eV). Raman spectroscopy experiments were implemented by Jobin-Yvon LabRAM HR 800 micro-Raman spectrometer using a 532 nm line from a He-Cd laser. The absorption spectra have been obtained using the PerkinElmer Lambda 950 spectrophotometer in dilute solution. The specific surface area were calculated by the Brunauer-Emmett-Teller (BET) method (TriStar II 3020, America).

Photocatalytic test. The photocatalytic performance of the as-synthesized D-BM composites were evaluated by degrading RhB and MB (organic pollutant of dye wastewater) under visible light irradiation. More details about the photocatalytic tests have been provided in ESI. In addition, transient photocurrent responses for the as-prepared catalysts were performed over an electrochemical analyzer (CHI660D Instruments, China) in a standard three electrode system. Under the irradiation of simulated sunlight (500 W Xe lamp with a cutoff filter), the prepared samples acted as working electrode (ITO as supporter). A Pt wire worked as counter electrode, and Ag/AgCl (saturated KCl) as reference.

Measurement of photoconductance. The photoconductance and photoresponse behavior of the D-BM was studied based on the nano-photodetectors. Typically, the disrupt Bi_2S_3@MoS_2 nanorods (NR-BM) from D-BM microspheres by oscillating (Sonics VCX800, America) were drop-deposited on the SiO_2 (300 nm)/Si substrate. Then the Au electrodes (100 μm × 150 μm) were defined on the NR-BM film by photolithography and high-vacuum electron beam (EB) evaporation process. The optoelectronic properties of the fabricated device were measured by a semiconductor parameter analyzer system (Keithley 4200-SCS) with the illumination laser of 650 nm.

Theoretical calculation. In the present work, the first-principles calculations of the heterogeneous structure have been performed, to provide the theoretical basis of the promoted photocatalytic activity. In details, the plane-wave pseudopotential calculations with the generalized gradient approximation (GGA) of Perdew-Burke-Ernzerhof (PBE) have been carried out using the Materials Studio 7.0 Package[61–63]. The cutoff kinetic-energy (Bi_2S_3 and MoS_2) are 600 eV/450 eV and the $3 \times 8 \times 3/5 \times 5 \times 1$ Monkhorst-Pack *k*-point mesh have been employed for the Brillouin-zone integration. The electronic structures were calculated with the optimized lattice geometries. Based on the convergence criteria, both energy and force were less than 10^{-5} eV and 0.01 eV $Å^{-1}$, for the fully relaxed initiating structures, respectively.

References

1. Zou, Z. G., Ye, J. H., Sayama, K. & Arakawa, H. Direct splitting of water under visible light irradiation with an oxide semiconductor photocatalyst. *Nature* **21,** 625–627 (2001).
2. Bian, T. *et al.* Spontaneous Organization of Inorganic Nanoparticals into Nanovesicles Triggered by UV Light. *Adv. Mater.* **26,** 5613–5618 (2014).
3. Feng, X. L. *et al.* Hollow Mesoporous Aluminosilica Spheres with Perpendicular Pore Channels as Catalytic Nanoreactors. *ACS Nano* **6,** 4434–4444 (2012).
4. Asahi, R., Morikawa, T., Ohwaki, T., Aoki, K. & Taga, Y. Visible-light photocatalysis in nitrogen-doped titanium oxides. *Science* **6,** 269–271 (2001).
5. Qin, N. *et al.* One-Dimensional CdS/TiO_2 Nanofiber Composites as Efficient Visible-Light-Driven Photocatalysts for Selective Organic Transformation: Synthesis, Characterization, and Performance. *Langmuir* **6,** 1203–1209 (2015).
6. Pu, Y. C. *et al.* Au Nanostructure-Decorated TiO_2 Nanowires Exhibiting Photoactivity Across Entire UV-visible Region for Photoelectrochemical Water Splitting. *Nano Lett.* **6,** 3817–3823 (2013).
7. Li, W. *et al.* Hydrothermal Etching Assisted Crystallization: A Facile Route to Functional Yolk-Shell Titanate Microspheres with Ultrathin Nanosheets-Assembled Double Shells. *J. Am. Chem. Soc.* **133,** 15830–15833 (2011).
8. Zhu, C. B. *et al.* A General Strategy to Fabricate Carbon-Coated 3D Porous Interconnected Metal Sulfides: Case Study of SnS/C Nanocomposite for High-Performance Lithium and Sodium Ion Batteries. *Adv. Sci.* **2,** 1500200 (2015).
9. Li, L., Li, P. F., Lu, N., Dai, J. & Zeng, X. C. Simulation Evidence of Hexagonal-to-Tetragonal ZnSe Structure Transition: A Monolayer Material with a Wide-Range Tunable Direct Bandgap. *Adv. Sci.* **2,** 1500290 (2015).
10. Wang, M. G., Han, J., Xiong, H. X. & Guo, R. Yolk@Shell Nanoarchitecture of Au@r-GO/TiO_2 Hybrids as Powerful Visible Light Photocatalysts. *Langmuir* **31,** 6220–6228 (2015).
11. Alessanodro, L. T. *et al.* Assembly, Growth, and Catalytic Activity of Gold Nanoparticles in Hollow Carbon Nanofibers. *ACS Nano* **6,** 2000–2007 (2012).
12. Zhang, Z. J., Wang, W. Z., Wang, L. & Sun, S. M. Enhancement of Visible-Light Photocatalysis by Coupling with Narrow-Band-Gap Semiconductor: A Case Study on Bi_2S_3/Bi_2WO_6. *ACS Appl. Mater. Interfaces* **4,** 593–597 (2012).
13. Guo, S. Q. *et al.* Mesoporous Bi_2S_3 nanorods with graphene-assistance as low-cost counter-electrode materials in dye-sensitized solar cells. *Nanoscale* **6,** 14433 (2015).
14. Elena, K. *et al.* Suppression of the Plasmon Resonance in Au/CdS Colloidal Nanocomposites. *Nano Lett.* **11,** 1792–1799 (2011).
15. Hong, T. *et al.* Anisotropic photocurrent response at black phosphorus-MoS_2 p-n heterojunctions. *Nanoscale* **7,** 18537 (2015).
16. Zhang, J., Liu, S. W., Yu, J. G. & Jaroniec, M. A simple cation exchange approach to Bi-doped ZnS hollow spheres with enhanced UV and visible-light photocatalytic H_2-production activity. *J. Mater. Chem.* **21,** 14655 (2011).
17. Malakooti, R. *et al.* Shape-Controlled Bi_2S_3 Nanocrystals and Their Plasma Polymerization into Flexible Films. *Adv. Mater.* **18,** 2189–2194 (2006).
18. Cademartiri, L. *et al.* Cross-Linking Bi_2S_3 Ultrathin Nanowires: A Platform for Nanostructure Formation and Biomolecule Detection. *Nano Lett.* **9,** 1482–1486 (2009).
19. Nambiar, S., Osei, E. K. & Yeow, J. T. W. Bismuth Sulfide Nanolflowers for Detection of X-rays in the Mammographic Energy Range. *Sci. Rep.* **5,** 9440 (2015).
20. Rath, A. K., Bernechea, M., Martinez, L. & Konstantatos, G. Solution-Processed Heterojunction Solar Cells Based on p-type PbS Quantum Dots and n-type Bi_2S_3 Nanocrystals. *Adv. Mater.* **23,** 3712–3717 (2011).
21. Tahir, A. A. *et al.* Photoelectrochemical and Photoresponsive Properties of Bi_2S_3 Nanotube and Nanoparticle Thin Films. *Chem. Mater.* **22,** 5084–5092 (2010).
22. Chen, G. H. *et al.* Fabrication of Ultrathin Bi_2S_3 Nanosheets for High-Performance, Flexible, Visible-NIR Photodetectors. *Small* **11,** 2848–2855 (2015).

23. Mesa, F., Dussan, A. & Gordillo, G. Study of the growth process and optoelectrical properties of nanocrystalline Cu_3BiS_3 thin films. *Phys. Status Solidi C* **7,** 917–920 (2010).
24. Chen, J. S. *et al.* Shape-controlled solvothermal synthesis of Bi_2S_3 for photocatalytic reduction of CO_2 to methyl formate in methanol. *Dalton Trans.* **42,** 15133 (2013).
25. Gao, X. H. *et al.* Formation of Mesoporous Heterostructured $BiVO_4/Bi_2S_3$ Hollow Discoids with Enhanced Photoactivity. *Angew. Chem. Int. Ed.* **53,** 5917–5921 (2014).
26. Yu, H. J., Huang, J., Zhang, H., Zhao, Q. F. & Zhong, X. H. Nanostructure and charge transfer in Bi_2S_3-TiO_2 heterostructures. *Nanotechnology* **25,** 215702 (2014).
27. Long, L. L., Zhang, A. Y., Huang, Y. X., Zhang, X. & Yu, H. Q. A robust cocatalyst Pd_4S uniformly anchored onto Bi_2S_3 nanorods for enhanced visible light photocatalysis. *J. Mater. Chem. A* **3,** 4301 (2015).
28. Manna, G., Bose, R. & Pradhan, N. Photocatalytic Au-Bi_2S_3 Heteronanostructures. *Angew. Chem. Int. Ed.* **53,** 6743–6746 (2014).
29. Jia, Y. N., Zhan, S. H., Ma, S. L. & Zhou, Q. X. Fabrication of TiO_2-Bi_2WO_6 Binanosheet for Enhanced Solar Photocatalytic Disinfection of *E.* coli: Insights on the Mechanism. *ACS Appl. Mater. Interfaces* **8,** 6841–6851 (2016).
30. Low, J. X., Cao, S. W., Yu, J. G. & Wageh, S. Two-dimensional layered composite photocatalysts. *Chem. Commun.* **50,** 10768–10777 (2014).
31. Zhou, W. J. *et al.* Synthesis of Few-Layer MoS_2 Nanosheet-Coated TiO_2 Nanobelt Heterostructures for Enhanced Photocatalytic Activities. *Small* **9,** 140–147 (2013).
32. Gong, Y. J. *et al.* Tellurium-Assisted Low-Temperature Synthesis of MoS_2 and WS_2 Monolayers. *ACS Nano* **9,** 11658–11666 (2015).
33. Wang, Q. H., Kalantar-Zadeh, K., Kis, A., Coleman, J. N. & Strano, M. S. Electronics and Optoelectronics of Two-Dimensional Transition Metal Dichalcogenides. *Nat. Nanotechnol.* **7,** 699–712 (2012).
34. Hong, T. *et al.* Polarized photocurrent response in black phosphorus field-effect transistors. *Nanoscale* **6,** 8978–8983 (2014).
35. Gao, Q. S., Giordano, C. & Antonietti, M. Electronics Oxygen Activation by MoS_2/Ta_3N_5 Nanocomposites for Selective Aerobic Oxidation. *Angew. Chem. Int. Ed.* **51,** 11740 (2012).
36. Perea-López, N. *et al.* CVD-Grown Monolayered MoS_2 as an Effective Photosensor Operating at Low-Voltage. *2D Mater.* **1,** 011004 (2014).
37. Min, Y. L., He, G. Q., Xu, Q. J. & Chen, Y. C. Dual-functional MoS_2 sheet-modified CdS branch-like heterostructures with enhanced photostability and photocatalytic activity. *J. Mater. Chem. A* **2,** 2578–2584 (2014).
38. Zhang, Y. *et al. In Situ* Fabrication of Vertical Multilayered MoS_2/Si Homotype Heterojunction for High-Speed VisibleCNearInfrared Photodetectors. *Small* **8,** 1062–1071 (2016).
39. Yoo, Y. D., Degregorio, Z. P. & Johns, J. E. Seed Crystal Homogeneity Controls Lateral and Vertical Heteroepitaxy of Monolayer MoS_2 and WS_2. *J. Am. Chem. Soc.* **137,** 14281–14287 (2015).
40. Xiao, J. *et al.* Exfoliated MoS2 Nanocomposite as an Anode Material for Lithium Ion Batteries. *Chem. Mater.* **22,** 4522–4524 (2010).
41. Wang, Y. C. *et al.* Electrochemical Control of Photoluminescence in Two-Dimensional MoS_2 Nanoflakes. *ACS Nano* **7,** 10083–10093 (2013).
42. Fan, X. B. *et al.* Fast and Efficient Preparation of Exfoliated 2H MoS_2 Nanosheets by Sonication-Assisted Lithium Intercalation and Infrared Laser-Induced 1T to 2H Phase Reversion. *Nano lett.* **15,** 5956–5960 (2015).
43. Wang, S. G. *et al.* A Facile One-Pot Synthesis of a Two-Dimensional MoS_2/Bi_2S_3 Composite Theranostic Nanosystem for Multi-Modality Tumor Imaging and Therapy. *Adv. Mater.* **27,** 2775–2782 (2015).
44. Wang, S. G. *et al.* Biocompatible PEGylated MoS_2 nanosheets: Controllable bottom-up synthesis and highly efficient photothermal regression of tumor. *Biomaterials* **39,** 206–217 (2015).
45. Li, Y. T. *et al.* Co-nucleus 1D/2D heterostructures with Bi_2S_3 nanowire and MoS_2 monolayer: One-step growth and defect-induced formation mechanism. *ACS Nano* **7,** 10083–10093 (2013).
46. Cui, W. Q., Shao, M. Y., Liu, L., Liang, Y. H. & Rana, D. Enhanced visible-light-responsive photocatalytic property of PbS-sensitized $K_4Nb_6O_{17}$ nanocomposite photocatalysts. *Applied Surface Science* **276,** 823–831 (2013).
47. Ren, X. P. *et al.* A Se-doped MoS_2 nanosheet for improved hydrogen evolution reaction. *Chem. Commun.* **51,** 15997–16000 (2015).
48. Shen, G. Z., Chen, D., Tang, K. B., Li, F. Q. & Qian, Y. T. Large-scale synthesis of uniform urchin-like patterns of Bi_2S_3 nanorods through a rapid polyol process. *Chem. Phys. Lett.* **370,** 334–337 (2003).
49. Tian, Y., Ding, T. T., Zhu, X. L., Tu, Y. F. & Zheng, G. Bi_2S_3 microflowers assembled from one-dimensional nanorods with a high photoresponse. *J. Mater. Sci.* **50,** 5443–5449 (2015).
50. Krichevsky, O. & Stavans, J. Correlated Ostwald Ripening in Two Dimensions. *Phys. Rev. Lett.* **70,** 1473 (1993).
51. Perera, S. D. *et al.* Hydrothemal Systhesis of Graphene-TiO_2 Nanotube Composites with Enhanced Photocatalytic Activity. *ACS Catal.* **2,** 949–956 (2012).
52. Rauf, A. *et al.* Facile Synthesis of Hierarchically Structured Bi_2S_3/Bi_2WO_6 Photocatalysts for Highly Efficient Reduction of Cr(VI). *ACS Sustainable Chem. Eng.* **3,** 2847–2855 (2015).
53. Daage, M. & Chianelli, R. R. Structure-Function Relations in Molybdenum Sulfide Catalysts: The "Rim-Edge" Model. *J. Catal.* **149,** 414–427 (1994).
54. Kumar, S., Khanchandani, S., Thirumal, M. & Ganguli, A. K. Achieving Enhanced Visible-Light-Driven Photocatalysis Using TypeII $NaNbO_3$/CdS Core/Shell Heterostructures. *ACS Appl. Mater. Interfaces* **6,** 13221–13233 (2014).
55. Romão, J. & Mul, G. Substrate Specificity in Photocatalytic Degradation of Mixtures of Organic Contaminants in Water. *ACS Catal.* **6,** 1254–1262 (2016).
56. Gao, Y. W., Wang, Y. & Zhang, H. Removal of Rhodamine B with Fe-supported bentonite as heterogeneous photo-Fenton catalyst under visible irradiation. *Appl. Catal., B: Environ.* **178,** 29–36 (2015).
57. Zhou, J. *et al.* Growth rate controlled synthesis of hierarchical Bi_2S_3/In_2S_3 core/shell microspheres with enhanced photocatalytic activity. *Sci. Rep.* **4,** 4027 (2014).
58. Luo, L. B. *et al.* Near-Infrared Light Photovolatic Detector Based on GaAs Nanocone Array/Monolayer Graphene Schottky Junction. *Adv. Funct. Mater.* **24,** 2794–2800 (2014).
59. Jie, J. S. *et al.* Photoconductive characteristics of single-crystal CdS nanoribbons. *Nano Lett.* **9,** 1887–1892 (2006).
60. Zhai, T. *et al.* Fabrication of High-Quality In_2Se_3 Nanowire Arrays toward High-Performance Visibe-Light Photodetectors. *ACS Nano* **4,** 1596 (2010).
61. Feng, N. *et al.* Magnetism by Interfacial Hybridization and *p*-type Doping of MoS_2 in Fe_4N/MoS_2 Superlattices: A First-Principles Study. *ACS Appl. Mater. Interfaces* **6,** 4587–4594 (2014).
62. Thomson, J. W. *et al.* Ultrathin Bi_2S_3 Nanowires: Surface and Core Structure at the Cluster-Nanocrystal Transition. *J. Am. Chem. Soc.* **132,** 9058–9068 (2010).
63. Wang, Y. *et al.* Syntheses, Growth Mechanism, and Optical Properties of [001] Growing Bi_2S_3 Nanorods. *J. Phys. Chem. C* **113,** 16009–16014 (2009).

Acknowledgements

One of the authors (M. J. Li) would like to thanks Prof. L. B. Luo, Y. Q. Yu, Dr. C. Li and H. L. Li for constructive discussions. This work was financially supported by Major State Basic Research Development Program of China (Grant No. 2013CB922300), the Natural Science Foundation of China (Grant Nos 11374097, 61376129, and

61504156), Projects of Science and Technology Commission of Shanghai Municipality (Grant Nos 15JC1401600, 14XD1401500, 13JC1402100, and 13JC1404200), and the Program for Professor of Special Appointment (Eastern Scholar) at Shanghai Institutions of Higher Learning.

Author Contributions

M.L. and Q.D. analysed data and prepared the manuscript and figures. M.L., P.Z., J.Z., and K.J. prepared the samples and performed experiments. M.L. and J.W. performed the first-principles calculations. The project was initiated and conceptualized by Z.H. and J.C. All authors reviewed the manuscript.

Additional Information

Supplementary information accompanies this paper at http://www.nature.com/srep

Competing financial interests: The authors declare no competing financial interests.

How to cite this article: Li, M. *et al.* Superior adsorption and photoinduced carries transfer behaviors of dandelion-shaped Bi_2S_3@MoS_2: experiments and theory. *Sci. Rep.* **7**, 42484; doi: 10.1038/srep42484 (2017).

Publisher's note: Springer Nature remains neutral with regard to jurisdictional claims in published maps and institutional affiliations.

This work is licensed under a Creative Commons Attribution 4.0 International License. The images or other third party material in this article are included in the article's Creative Commons license, unless indicated otherwise in the credit line; if the material is not included under the Creative Commons license, users will need to obtain permission from the license holder to reproduce the material. To view a copy of this license, visit http://creativecommons.org/licenses/by/4.0/

© The Author(s) 2017